Exp.-Nr.: A1/02–16
Eingang:

Mainz Microtron MAMI

Collaboration: A1

Spokesperson: H. Merkel

Proposal for an experiment

The initial state radiation experiment with a jet target

Collaborators:

A. B. Weber[1], P. Achenbach[1], S. Aulenbacher[1], J. C. Bernauer[2], D. Bosnar[3], T. Brecelj[4], L. Correa[5], A. Denig[1], M. O. Distler[1], A. Esser[1], H. Fonvieille[5], I. Friščić[2,3], K. Griffioen[6], M. Hoek[1], S. Kegel[1], Y. Kohl[1], H. Merkel[1], M. Mihovilovič[1,4], J. Müller[1], U. Müller[1], J. Pochodzalla[1], B. S. Schlimme[1], M. Schoth[1], C. Sfienti[1], S. Širca[4,7], S. Štajner[4], M. Thiel[1], M. Vanderhaeghen[1],

[1] Institut für Kernphysik, Johannes Gutenberg-Universität Mainz, Germany
[2] Massachusetts Institute of Technology, Cambridge, USA
[3] Department of Physics, University of Zagreb, Croatia
[4] Jožef Stefan Institute, Ljubljana, Slovenia
[5] Clermont Université, Université Blaise Pascal, Clermont-Ferrand, France
[6] College of William and Mary, Williamsburg, VA, USA
[7] Department of Physics, University of Ljubljana, Slovenia

Contact persons:

H. Merkel (merkel@kph.uni-mainz.de),
M. Mihovilovič (miham@kph.uni-mainz.de)

Abstract

We propose a new, high precision measurement of the proton charge form-factor at very small momentum transfers in order to provide new insight into the discrepancy between different measurements of the proton charge radius. Although the newest (unofficial) value from hydrogen spectroscopy is in agreement with the equivalent measurements in the muonic-hydrogen and indicates a reconciliation of the puzzle, the discrepancy with the results from the nuclear scattering experiments remains unexplained. Several latest reanalyses of available scattering data are offering radii that are consistent with the spectroscopic results, but the physics community is divided on whether these solutions can be trusted or not. To conclusively solve the puzzle and bring dispute to a closure, new measurements of the proton charge form-factors are therefore needed in the region of extremely small Q^2, where data are most relevant for the proton radius. To reach this goal the experiment will use a novel, but proven technique based on the initial-state-radiation, which avoids kinematical limitations that restrict traditional elastic scattering measurements to $Q^2 \approx 3 \cdot 10^{-3}\,\mathrm{GeV}^2/\mathrm{c}^2$ and offers the possibility to extract form factors at $Q^2 \geq 1 \cdot 10^{-4}\,\mathrm{GeV}^2/\mathrm{c}^2$ using standard experimental equipment. The experiment will be performed at the A1 experimental hall using MAMI-B electron beam with energies of 195 MeV, 330 MeV, 400 MeV and 495 MeV in combination with a gaseous hydrogen jet target and the standard three spectrometer setup. We ask for 30 days of beam-time with 15 days of installation time to measure cross-sections at 47 different kinematic points in the radiative tail with statistical precision of 0.2 %.

Contents

1 Physics overview and motivation **4**
1.1 Nuclear scattering experiments 5
1.2 Reanalyses of the scattering data 6
1.3 Hydrogen spectroscopy 6
1.4 Muonic hydrogen Lamb shift measurement 8
1.5 Latest developments 8

2 Proposed measurement **9**
2.1 The concept of Initial State Radiation method 9
2.2 Monte-Carlo simulation 10
2.3 Experiences from the past measurements 12
2.4 Improvements for the next experiment 15
2.4.1 Hypersonic jet target 15
2.4.2 Helium balloon 15
2.5 Proposed kinematics and beam-time requests. 17
2.6 Systematic uncertainty 20

1 Physics overview and motivation

The proton has been studied since the early days of experimental hadronic physics [1]. Through the years many different measurements of its properties have been performed, ranging from the pioneering experiments in the 1960s to the high precision measurements done in the last years. In particular, its radius has been determined by various electron scattering experiments and many atomic Lamb shift measurements (see Figure 1). Both approaches gave consistent results. Unfortunately their average does not agree with the findings of the very precise Lamb shift measurements in muonic-hydrogen [2, 3], which report a 8σ smaller value for the proton charge radius.

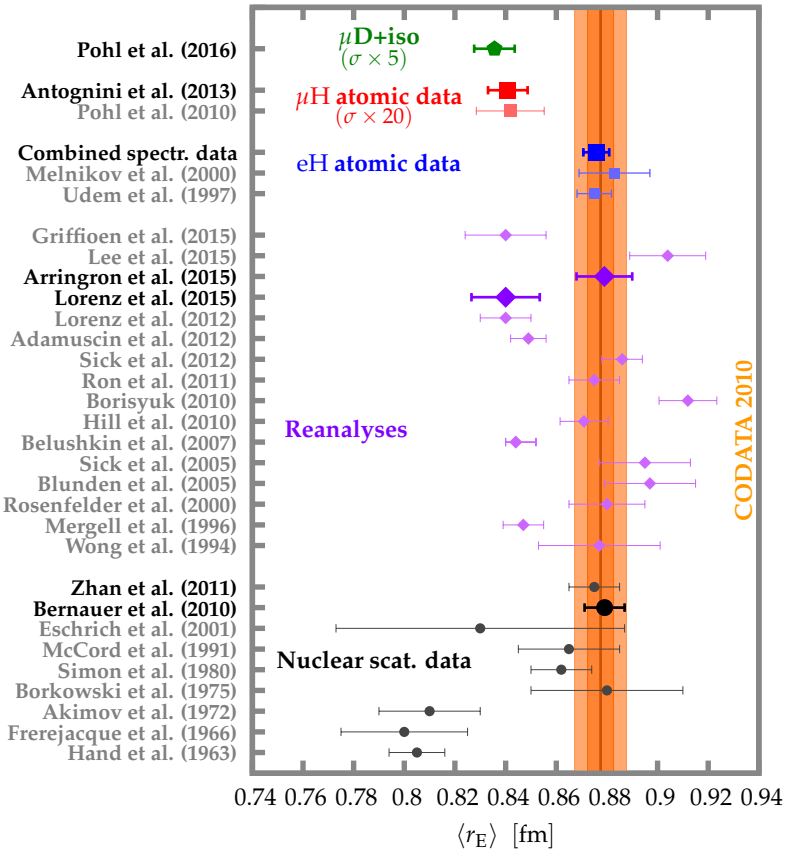

Figure 1 — An overview of the available proton charge radius measurements. Full circles show findings of the scattering experiments. Full squares represent values obtained from the Lamb shift spectroscopy. The values determined from the muonic hydrogen (deuterium) measurements are colored red (green). The uncertainties of muonic hydrogen (deuterium) data are multiplied by factor 20 (5) for clarity [4].

The observed discrepancy created a great excitement in the physics community, because it puts QED and our understanding of the nuclear physics to a rigorous test. Since the observation of the inconsistency in 2010, various explanations for it have been offered.

The most trivial explanation would be an unidentified error in the existing measurements. However, both spectroscopic and nuclear scattering measurements have been reexamined and no problem has yet been found. Furthermore, all measurements except the muonic-hydrogen measurement were done by different groups and they all mutually agree. However, if it turns out, that the old measurements indeed are erroneous, then a new value of the radius would command also a different value of the Rydberg constant (due to a strong correlation between the two parameters). This would have a strong impact on all existing spectroscopic results [5].

A mistake in the existing calculations used to interpret spectroscopic measurements or an overlooked higher order term also do not appear to be a plausible scenario. The calculations were made by several theoretical groups using different approaches and they all get very similar results [6]. They invested a large effort to examine many different Feynman diagrams and the

current consensus is that a missing higher order term is not responsible for the discrepancy, because they all contribute much less than the needed $300\,\mu$V [7]. Hence, this could suggest a hidden problem with a leading (vacuum polarization) term, or it could even be an indication of a fundamental problem with QED.

People have offered also many other explanations, ranging from the incomplete two-photon corrections to the contributions of the molecular ions. However, the most intriguing ideas are those claiming that the discrepancy can not be explained within the framework of Standard Model. The idea of a new force and corresponding mediator particle that breaks the electron-muon universality is interesting also because it could simultaneously explain the muonic $(g-2)_\mu$ puzzle [8]. A promising candidate for a mediator particle is a U(1) gauge boson that moderates the interaction between the dark matter and the standard model particles. Unfortunately, no such particle has been found yet [9].

1.1 Nuclear scattering experiments

In a typical scattering experiment is the radius of a proton determined indirectly by measuring the cross-section for elastic scattering of electrons on hydrogen [10]. The measured cross-section depends on electric and magnetic form-factors, G_E^p and G_M^p, which carry information about the charge and magnetization distribution in the proton and are extracted from the measured data via Rosenbluth separation. The charge radius is extracted from the slope of the electric form-factor at $Q^2 = 0$:

$$r_E^2 \equiv -6\hbar^2 \frac{d}{dQ^2} G_E(Q^2)\bigg|_{Q^2=0},$$

where Q^2 represents the square of the momentum transfer four-vector. Unfortunately, the data for $Q^2 < 0.004\,(\mathrm{GeV}/c)^2$ that would allow for a reliable and precise determination of this slope do not yet exist [11]. Therefore, an extrapolation of available G_E^p points to $Q^2 \to 0$ is used to estimate r_E^2. The extracted value of r_E^2 is extremely sensitive to the details of this extrapolation, which in turn strongly depends on the precision and accuracy of the values of G_E^p themselves.

The first determination of the radius from nuclear scattering data was performed by Hand et al., who considered preexisting measurements of the cross-section from the Stanford Linear Accelerator [12]. In their publication they recognised the advantages of extracting the Sachs charge and magnetisation form-factors (GE and GM) from the measured elastic cross-sections and their direct connection to the mean charge and magnetisation radii of the nucleon (nucleus). This first analysis was then followed by different dedicated measurements of the radius [13, 14, 15, 16, 17, 18, 19]. However, currently the best extraction of the radius from the nuclear scattering data is the one of Bernauer [20]. In this experiment at the A1 the elastic cross-section was measured, for 1400 different kinematic points, covering the Q^2 from $1\,(\mathrm{GeV}/c)^2$ down to as low as $4\cdot 10^{-3}\,(\mathrm{GeV}/c)^2$ with the statistical uncertainty smaller than $0.2\,\%$. The smallest Q^2 was restricted by the minimal available beam energy of the accelerator and the minimal scattering angle, to which magnetic spectrometers can be positioned to. In the analysis the measured points were not sorted in terms of Q^2 and used in the Rosenbluth separation. Instead, an alternative approach was considered, where models for the elastic form-factors were fitted directly to all measured points [21]. Various models were tested which all gave similar results with $\chi^2/1400 \approx 1.14$. The obtained fit for $G_E^p(Q^2)$ could then be directly used to estimate the proton charge radius. The best estimate for the proton charge radius was determined to be $r_E^{\mathrm{Scat.}} = (0.879 \pm 0.008)\,\mathrm{fm}$.

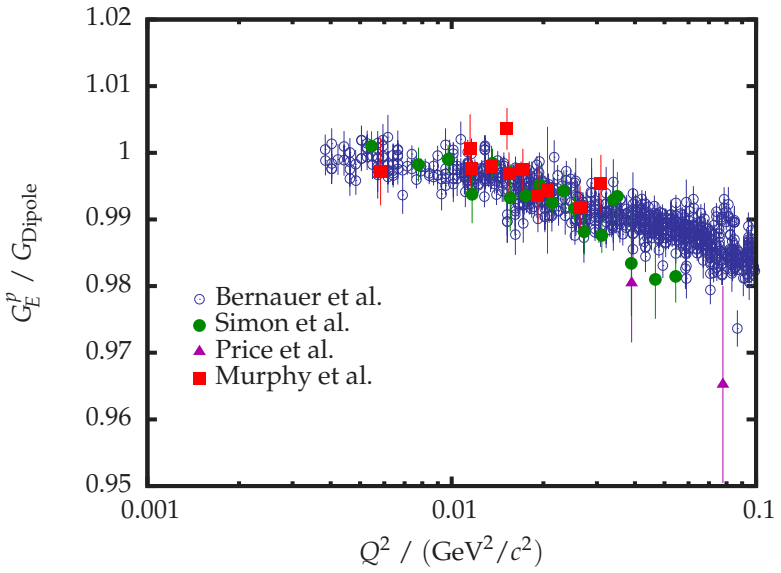

Figure 2 — Available data on the charge form factor at $Q^2 \leq 0.1\,\mathrm{GeV}^2/c^2$, relative to the standard dipole approximation. The existing measurements are already very precise but even the best experiments provide data only for $Q^2 \geq 4 \cdot 10^{-3}\,\mathrm{GeV}^2/c^2$. To calculate the radius, the data therefore need to be extrapolated towards zero. To avoid complications with extrapolations and unwanted biases of the extracted radius, data at even smaller Q^2 are needed.

Measuring the cross-section for elastic scattering of electrons off protons is not the only way to reach information on the charge form-factor. Additional insight about the G_E^p can be obtained by measuring the form-factor ratio G_E^p/G_M^p in a coincident double polarisation experiments, using recoil polarimetry. This technique is free of backgrounds and allows for precise measurement of the ratio. Such experiments have been performed at MAMI [22] and at Jefferson Lab [23, 24]. The most recent measurement was performed by Zhan et al., where they determined the ratio for the four-momentum transfer Q^2 between 0.3 and $0.7\,(\mathrm{GeV}/c)^2$ with the total uncertainty of approximately 1 %. Results of this experiment clearly showed a deviation of the ratio from unity, indicating that the charge is distributed differently in the nucleus than magnetisation. The obtained ratios were then combined with the available world data on G_E^p and G_M^p (Bernauer data excluded) in order to extract the proton electric radius of (0.875 ± 0.010) fm.

1.2 Reanalyses of the scattering data

The publications reporting on measurements of the proton-charge radius are accompanied by different re-analyses of the existing nuclear scattering results. They consider additional effects in the interpretation of the measured data or offer an alternative approach for extracting the radius. Some of the analyses remains consistent with the CODATA value [25, 26, 27], However, there is a series of recent publications, which obtain results, that are in agreement with the muonic-hydrogen results [28, 29, 30, 31], but are being continuously criticised for not correctly interpreting the data and for using only low Q^2 data, which causes their fits to be biased [32, 33, 34].

1.3 Hydrogen spectroscopy

The spectroscopy of the hydrogen atom plays an important role in the development of the modern physics, because it can be used to precisely test the predictions of the theory of Quantum Electrodynamics (QED). The theory has two free parameters, the Rydberg constant (R_y) and the mean charge radius of the proton which need to be determined elsewhere (for instance in the scattering experiments) before being able to confront it to precise atomic data. Alternatively, one could

decide to trust QED and combine it with the measured spectroscopic spectra to extract these two parameters, thus offering a complementary way of determining the proton charge radius.

An important effect on the atomic levels is the Lamb shift [35], a small energy level splitting in hydrogen, which arises due to the vacuum fluctuations. In the first approximation the effect is proportional to the probability of finding an electron with the principal and orbital quantum numbers (n,l) at the center of the atom:

$$\Delta E^{nl}_{\text{Lamb}} \propto |\Psi_{nm}(0)|^2 \,.$$

Figure 3 shows the electron probability distributions $|\Psi_{nm}(\vec{r})|^2$ in the hydrogen atom for first few quantum numbers. In the S-states electron spends most of its time at the center, resulting in a non-zero Lamb correction. Hence, the energy levels for the S-states will shift due to this effect. On the other hand, for the P- and D-states, the probability for finding electron at the center is almost zero, which leads to a negligible shift of these energy levels.

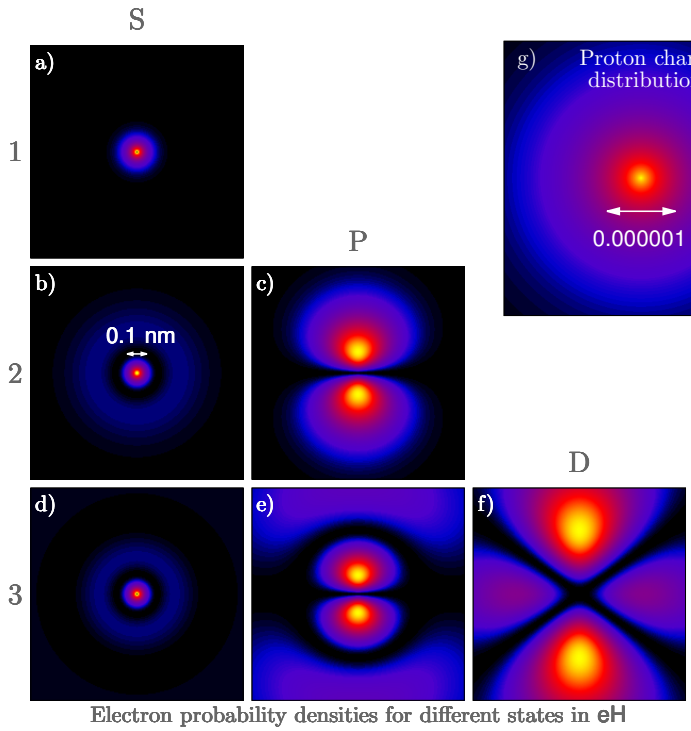

Figure 3 — a-f) Projections of the probability densities for an electron in the hydrogen atom to the xz-plane. The results are shown for electrons with principal quantum number $n = 1,2,3$ and orbital quantum numbers $l = S,P,D$. g) The proton charge distribution at the center of the hydrogen atom.

Moreover, one should also consider that the center of the atom is not empty, but is occupied by a proton with a finite size, which brings additional term to the Lamb shift that depends on the proton radius. This is usually a small correction to the total Lamb shift, but it is in fact the very term that is exploited to determine the proton radius. Disregarding the hyperfine coupling, new energy levels of the nS-states can be written as:

$$E(n,l=S) \cong -\frac{R_y}{n^2} + \frac{\Delta E^{1S}_{\text{Lamb}}}{n^3}\,, \;\; \Delta E^{1S}_{\text{Lamb}} \cong \left(8.172 + 1.56\left(\frac{r_E}{\text{fm}}\right)^2\right) \text{MHz}\,. \tag{1}$$

Equation (1) offers many possibilities how to perform the spectroscopic measurements. For example, when one is interested only in the Lamb shift and radius, a measurement of the energy difference $\Delta E_{2S\to 2P}$ for the $2S \to 2P$ transition could be performed, because then the first term in (1) dissapears and only Lamb terms survive. Alternatively, one could combine results of the $1S \to 2S$ and $1S \to 3S$ transitions and then exploit the different n-dependence of the two terms in (1) to simultaneously extract both the Rydberg constant and the proton charge radius. Using this

philosophy many different transitions have been measured by many different groups [36], which all together give a mean value for the proton charge radius of (0.8758 ± 0.0077) fm. Combining this result with the findings of selected scattering experiments, one obtains the recommended CODATA value for the radius, which equals to $r_E^{\text{CODATA}} = (0.8775 \pm 0.0051)$ fm.

1.4 Muonic hydrogen Lamb shift measurement

The precision of the hydrogen spectroscopy measurements is comparable to the precision of the findings of the nuclear scattering experiments. However, they are both inferior to the results of the muonic hydrogen Lamb shift measurement. A muon, being 200-times heavier than the electron, is confined to a much smaller orbit around the proton. This increases the overlap between the two and significantly amplifies the Lamb shift. The full QED calculation predicts the following energy difference for the $2S \rightarrow 2P$ transition [36]:

$$\Delta E_{\text{Lamb}}^{\mu\text{H}} = \left(209.9779 - 5.2262 \left(\frac{r_E}{\text{fm}} \right)^2 + 0.0347 \left(\frac{r_E}{\text{fm}} \right)^3 \right) \text{meV}. \tag{2}$$

According to (2) the contribution of the proton finite size represents only 1.8 % of the whole shift, which is much smaller than in the case of electronic (normal) hydrogen, where the proton part represents 15 % of the Lamb shift. However, the Lamb effect is now 100-times larger than in electronic hydrogen, which allows for much more precise determination of the proton charge radius. Furthermore, muonic and electronic hydrogen differ also in the sign of the Lamb shift, because different Feynman diagrams govern the corrections. In the electronic hydrogen the effect is dominated by the lepton vertex correction diagram, while in the muonic hydrogen, vacuum polarization represents the leading term.

The first successful measurement of the Lamb shift in muonic hydrogen was done at Paul Scherrer Institute (PSI) [2], using a moderated beam of muons incident on the hydrogen target. In the collisions highly excited muonic hydrogen atoms were created. Most of them decayed directly to the $1S$ state, while 1% of the muons de-excited to the $2S$ state. A tunable pulsed laser was then used to excite these states to the $2P$ level. If the frequency of the laser was right and the transition was successful, the $2P$ states de-excited to the $1S$ state, emitting 2 keV X-rays that were detected by photo-diodes. In the experiment a sharp peak at approximately 50 THz was observed, which corresponds to a Lamb shift of $\Delta E_{Lamb}^{\mu\text{H}} = 206.2949(32)$ meV. This value, combined with the QED calculations given in (2), yields a very precise value for the proton charge radius ($r_{\text{E}}^{\mu\text{H}} = (0.84184 \pm 0.00067)$ fm) which is 4 % (or 7.9σ) smaller than the CODATA value.

1.5 Latest developments

The proton radius problem stimulated many new experiments, trying to bring new insight into the matter. The initial state radiation program at MAMI, discussed in this proposal, is competing with a "pRad" experiment at Jefferson Lab [37], which also measures proton-charge form-factor in an electron scattering experiment. The experiment uses a non-magnetic detector system in combination with a windowless gas target, which gives possibility to measure elastic-cross sections at very forward angles ($\approx 5^\circ$) , thus reaching form-factors at $Q^2 \approx 2 \cdot 10^{-4}\,\text{GeV}^2/c^2$. The experiment was successfully accomplished in June 2016 and since then the analysis of the data is in progress.

To test the BSM hypotheses which explain the proton radius discrepancy by breaking the lepton universality, MUSE [38] collaboration aims to precisely measure proton charge form-factor with muon and electron beams of both polarities at Q^2 as low as $2 \cdot 10^{-3}\,\mathrm{GeV}^2/c^2$. The measured ratio will directly show if muons indeed interact differently with protons than electrons. Additionally, they will be able to test the two-photon-exchange contributions, which are relevant for the form-factor measurements at higher Q^2. The experiment was successfully approved by the funding agencies this year and is expected to run in 2018-2019.

Together with the scattering experiments different new spectroscopic measurements are also underway. The most recent result comes from the CREMA collaboration, which reports on a new precise measurement of the deuteron radius from the laser spectroscopy of muonic deuterium [5]. Their result is $7.5\,\sigma$ smaller than the CODATA value. Even more importantly, when combined with the measurement of isotope shifts in $1S-2S$ transition, which determines the squared deuteron-proton charge difference

$$r_d^2 - r_p^2 = 3.82007(65)\,\mathrm{fm}^2\,,$$

they extract the proton radius of $0.8356(20)\,\mathrm{fm}$, which supports "the smaller version proton" and thus even further amplifies the proton radius puzzle (See Fig. 1). The new publication also offers a potential solution for the problem by changing the Rydberg constant. If the Rydberg constant would be wrong for 7σ because of a yet undiscovered, common systematic effect in the spectroscopic measurements of transitions in hydrogen and deuterium, then such change would shift hydrogen to a smaller μp value. It would also bring the deuterium radius to 2.5σ of the μd value and make the whole picture somehow consistent. Therefore the collaboration also preformed the measurements in the hydrogen, from which both Rydberg constant and radius could be extracted. Their preliminary and unpublished results seem to support the offered explanation.

If this turns to be the correct explanation, then together with the latest fits of Griffieon or Higinbotham one could undestand this as a reconciliation of the problem. However, scuh conclusions should not be drawn to quickly! The community is, as discussed above, still divided on the interpretation of the nuclear scattering results. Furthermore, additional spectroscopic measurements need to be done, preferably by different groups, to confirm/deny the hypothesis of a smaller Rydberg constant. With the potential solution on the horizon, it is therefore crucial, now more than ever, to provide new precise spectroscopic and scattering data in order to find a consistent/final answer for the problem.

2 Proposed measurement

We propose a new measurement of proton charge form factor using a novel experimental approach based on the initial state radiation. The employed technique was inspired by a similar method used in high energy physics [39] and offers possibility to investigate proton structure at $Q^2 \geq 2 \cdot 10^{-4}\,\mathrm{GeV}^2/\mathrm{c}^2$ using standard experimental equipment.

2.1 The concept of Initial State Radiation method

The radiative tail of an elastic peak observed in the measured nuclear spectra is dominated by contributions of two Bethe-Heitler diagrams [40] shown in Figure 4. The initial state radiation

diagram (BH i) describes the process where the incident electron emits a real photon before interacting with the proton. Since the emitted photon carries away part of the incident energy, the momentum transferred to the proton (Q^2_{Vertex}) is decreased. Hence, this process opens the possibility to probe the proton structure at values of $Q^2_{\text{Det}} = Q^2_{\text{Vertex}}$ that are smaller than the value fixed by the experimental kinematics. On the other hand, the final state radiation diagram (BH f) corresponds to the reaction where the real photon is emitted only after the interaction with the nucleon. Consequently, Q^2_{Vertex} at the vertex remains constant, while the detected $Q^2_{\text{Det}} \leq Q^2_{\text{Vertex}}$ changes.

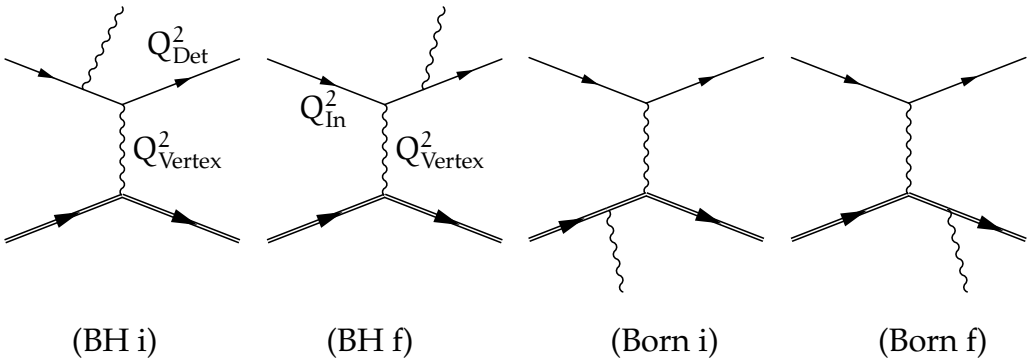

Figure 4 — Feynman diagrams for inelastic scattering of electron off a proton, where the electron and proton emit real photons before or after the interaction. Diagrams where electrons emit a photon are known as Bethe-Heitler (BH) diagrams, while those where protons emit real photons are called Born diagrams. The Q^2_{Vertex} represents the square of the four-momentum transferred to the hadron. The Q^2_{In} is the momentum fixed by the beam energy and the scattering angle, while the $Q^2_{\text{Det}} \leq Q^2_{\text{In}}$ corresponds to value measured with the detector. For the (BH-i) $Q^2_{\text{Vertex}} = Q^2_{\text{Det}}$, and for the (BH-f) $Q^2_{\text{Vertex}} = Q^2_{\text{In}}$.

In an experiment only Q^2_{Det} can be measured, which means that looking only at data, initial state radiation processes can not be distinguished from the final state radiation. To reach information corresponding only to the initial state radiation, measurements need to be studied together with results of a Monte-Carlo simulation. This is the basic idea of the discussed MAMI experiment, which aims to extract G^p_E in the range $10^{-4} \leq Q^2_{\text{Vertex}} \leq 0.005\,(\text{GeV}/c)^2$.

2.2 Monte-Carlo simulation

A comprehensive Monte-Carlo simulation is a key part of this experiment. Relaying on a detailed description of the processes contributing to the radiative tail, the simulation could be directly compared to the data. Since the form-factor is the only free parameter of the simulation, the discrepancy between the data and the simulation at the given Q^2 could be directly attributed to the deviation of the predicted form-factor from the true value.

The simulation is based on the standard A1 simulation package, which has been proven to work well for a serious of past experiments and includes a detailed description of the spectrometer setup. For our experiment the framework was utilized in combination with a sophisticated generator of events, that was written originally for the estimation of the background in the VCS experiments [41, 40]. This generator exactly calculates the amplitudes for the Bethe-Heitler diagrams and two Born terms, where initial and final proton emit real photons. This is crucial for a precise description of the radiative tail far away from the elastic line, where the typically used peaking approximations become imprecise (see Fig. 5).

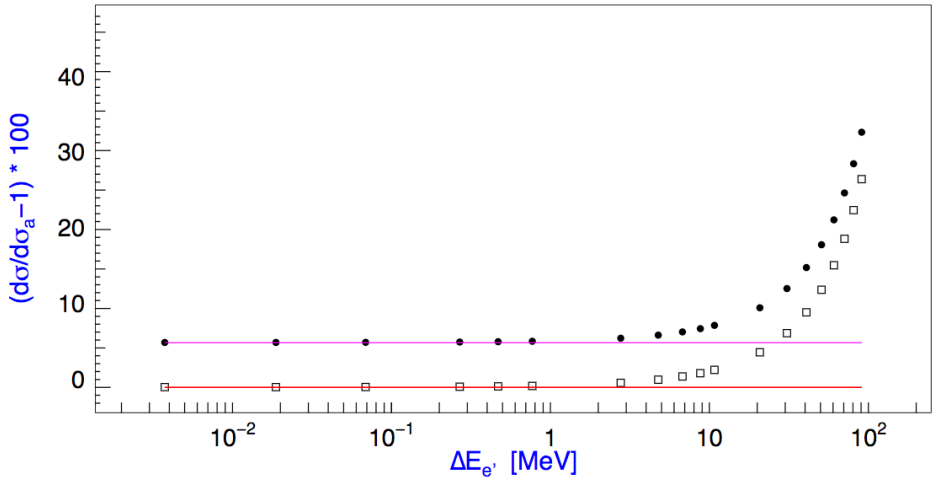

Figure 5 — Difference between the full calculation of radiative corrections and the soft-photon approximation. Open squares show results when only radiation from the electron is considered (BH-i+BH-f). Full circles demonstrate results when both radiation from electron and proton are taken into account. Corresponding soft photon results are shown with straight lines [40]. Once more than few MeV from the elastic line, the peaking approximations become inadequate for the precise extraction of the form-factors that ISR experiment is after.

It turns out that for a sub-percent description of the radiative tail 100 MeV away from the elastic line, both real and virtual next-to-leading order terms also need to be considered. For the virtual leptonic corrections we are using the calculations of Vanderhaeghen [40]. Since the calculation of these contributions requires a lot of computation power, we evaluated them in a separate program and then add them as effective corrections to the cross sections [42]. Additionally, in the calculation of the vacuum polarisation corrections only electrons are considered. The muonic loop corrections represent a per-mill effect and are considered only in the estimation of the systematic uncertainty. For the calculation two-photon emission diagrams we are using corrections that are based on the elastic peaking approximation. The external radiative corrections are based on the calculations of Mo and Tsai [43, 44], which are accurate to 1 % level. The corrections on the proton side are expected to be small, since we are measuring at low Q^2. This allows us to approximate them with the elastic approximation of Maximon-Tjon [45]. Furthermore, we consider only part where proton is on the shell. The off-shell part, that requires calculation of the VCS amplitudes is being neglected.

In the analysis the simulation will be run for different parameterizations of form-factors. The best value for G_E^p at each Q^2 will then be determined via χ^2-minimization of difference between the data and the simulation. The contribution of G_M^p to the total cross-section is for all settings smaller than 4 % and will be therefore approximated with the standard dipole approximation.

The results of the full Monte-Carlo simulation, which includes all the above corrections is presented in Fig. 7. For each of the kinematics the elastic peak and its two radiative tails are clearly visible. The diagonal tail corresponds to initial state radiation, while the horizontal one belongs to final state radiation.

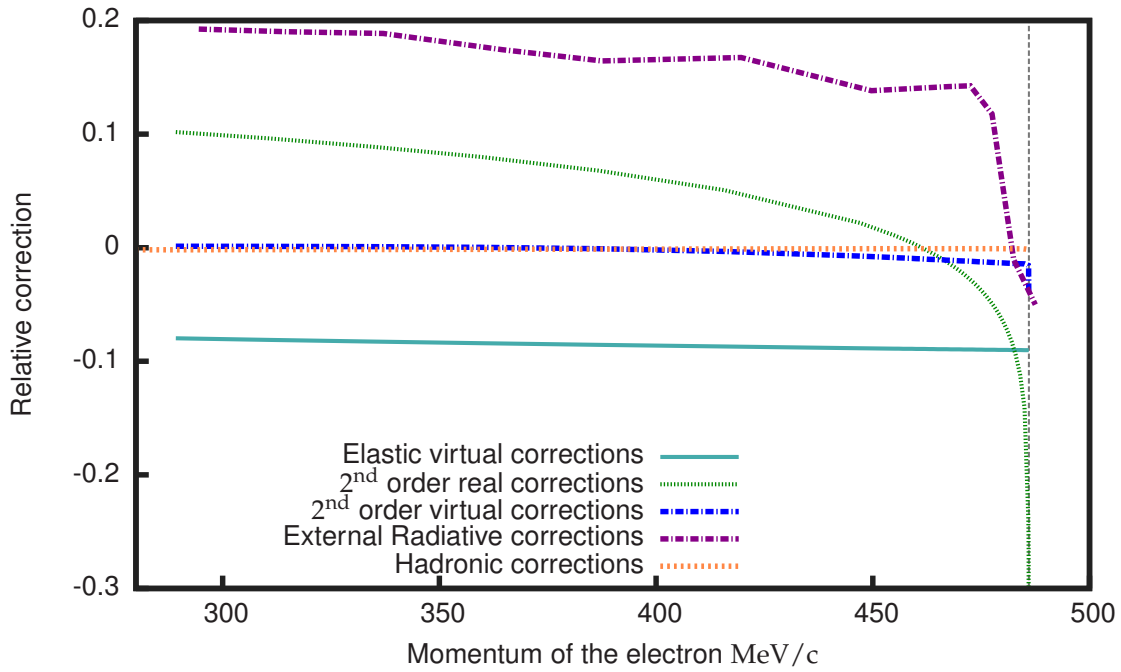

Figure 6 — Comparison of the next-to-leading order corrections that are included in the simulation as effective corrections to the cross-section. The most important are the real and virtual corrections on the lepton side, and the external corrections, which are all of order of 10 %. The ISR experiment depends only on the relative changes of the corrections. In the tail all of them are more less flat. However, near the elastic peak, the corrections, where photons are emitted, start to change very rapidly.

2.3 Experiences from the past measurements

The proposed experiment is not the first of its kind. The idea for such experiment originates in 2010 when the first pilot measurement was performed at the spectrometer hall of the A1 Collaboration, in order to check the feasibility of such measurement. For the measurement rastered electron beam with energies of 195 MeV, 330 MeV and 495 MeV was used in combination with a liquid Hydrogen target. For cross-section measurements spectrometer B was employed. It was positioned at a fixed angle of 15.25°, while its momentum settings were being adjusted to scan the complete radiative tail for each energy setting. Kinematic settings were chosen such that the radiative tails of all three setting overlapped (see Figure 7). In total, 60 different setups were investigated, resulting in three weeks of data taking: two weeks for production measurements and one week for empty-cell measurements, needed for proper background subtraction. Beam currents were between 10 nA and 1 μA, depending on the setup and were measured by two probes: the non-invasive Förster probe and the invasive pA-meter. Unfortunately at low beam currents and low beam energies neither of the probes was accurate enough. Hence, spectrometer A, positioned at a fixed setting, was employed for precise monitoring of beam luminosity.

The collected data revealed a strong contamination of the data with the cryogenic depositions, which gathered around the target cell due to limited vacuum in the scattering chamber. These additional layers, consisting mostly of solid nitrogen and oxygen, distored the measured spectra to a level, that radiative tail could not be measured. Therefore, another experiment was performed in 2013, where huge attention was given to minimising these effects. The problem was addressed by replacing the windows of the scattering chamber with new Kapton windows that were enforced with an additional layer of aramid foils. They ensured more than two order of magnitude better vacuum and this way significantly smaller contributions of cryogens to the spectra, allowing

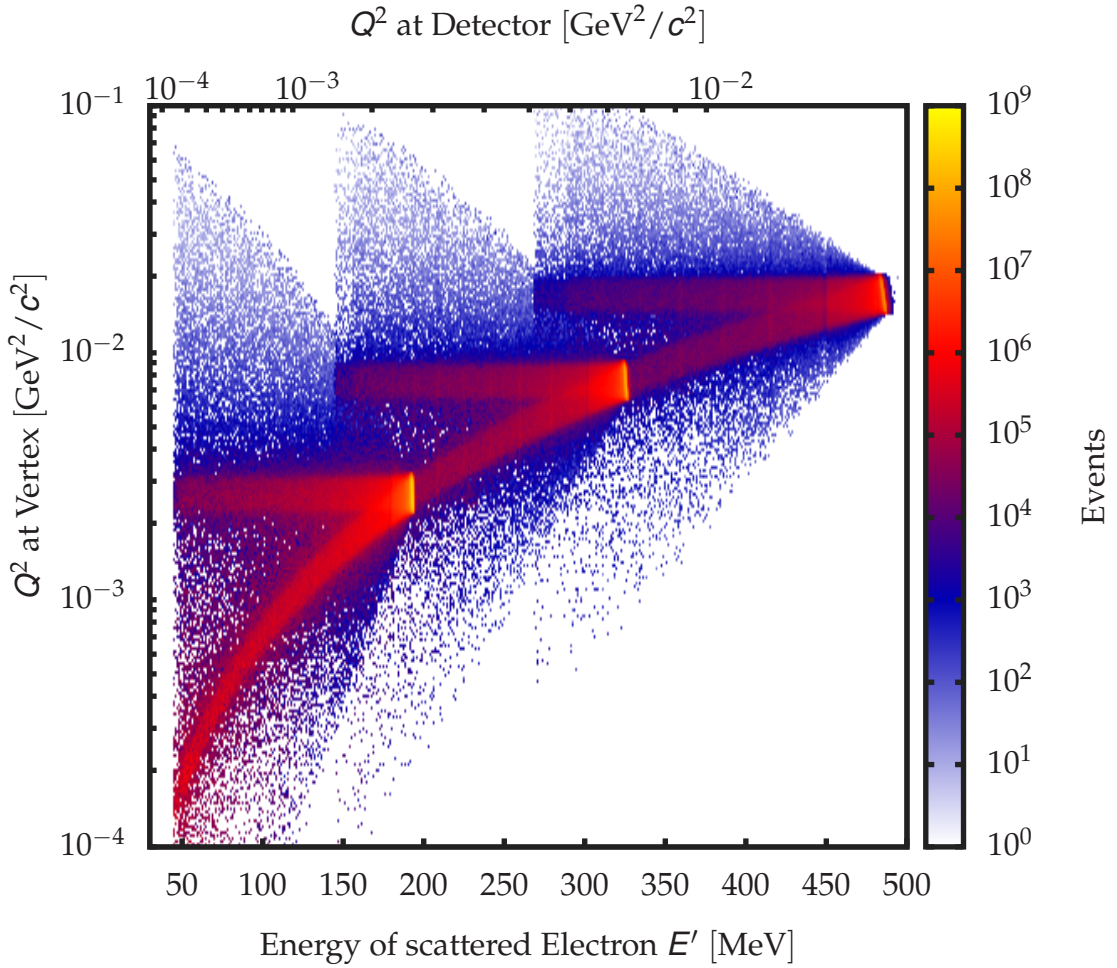

Figure 7 — Results of Monte-Carlo simulation for experimental settings with beam energies 195 MeV, 330 MeV and 495 MeV. The plot shows the detected rates as a function of Q^2_{Vertex} at the vertex and Q^2_{Det} or energy of scattered electron which are directly measured by the spectrometer. Diagonal and horizontal tails in each settings are caused by initial state and final state radiation, respectively.

precise measurement of the radiative tail.

The 2013 experiment was performed in the same way as the 2010 measurement, with almost identical set of kinematical configurations. The only significant difference was a newly installed automatic beam position control unit, that experiment benefited a lot from. This computer module communicated with MAMI and every three minutes automatically measured beam position and then made corrections if necessary. Additionally, it also measured beam current using invasive pA meter which all together gave us incredibly stable beam conditions. The experiment successfully recorded data for Q^2 ranging from $2 \cdot 10^{-2}\,(\mathrm{GeV}/c)^2$ down to only $2 \cdot 10^{-4}\,(\mathrm{GeV}/c)^2$ without major experimental difficulties.

Unfortunately only a detailed offline analysis then revealed hidden backgrounds coming from the bulk material of the target and the entrance flange of the spectrometer. Elastic events which are a priori outside the spectrometer's acceptance and were blocked by the bulk material of the spectrometer and target, underwent a secondary scattering process in the metal and rescattered back into its acceptance. While the effect was tiny at high energies, these additional events significantly distorted measured spectra at low energies and consequently limited the analysis to $1 \cdot 10^{-3}\,(\mathrm{GeV}/c)^2$.

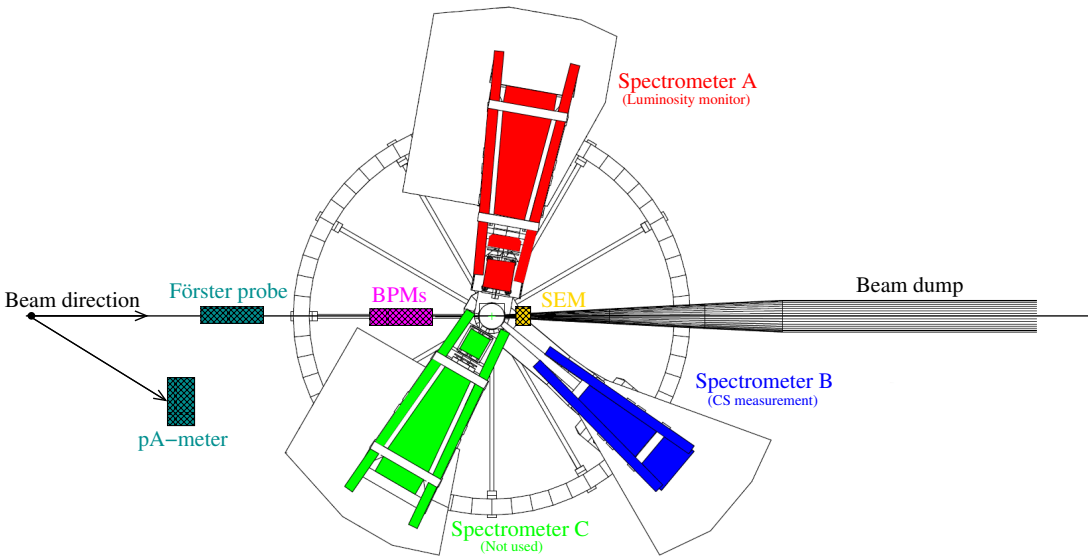

Figure 8 — Three spectrometer setup at MAMI [46]. Spectrometer A is employed as luminosity monitor, while spectrometer B is used for cross-section measurements. Beam current is measured with non-invasive flux-gate magnetometer (Förster probe) and invasive calorimeter (pA-meter), both located inside the MAMI accelerator. Beam position is determined with two beam position monitors (BPMs) mounted right in front of the target. In the 2013 experiment a secondary electron emission monitor (SEM) was mounted in front of the beam dump as a supplementary beam current monitor.

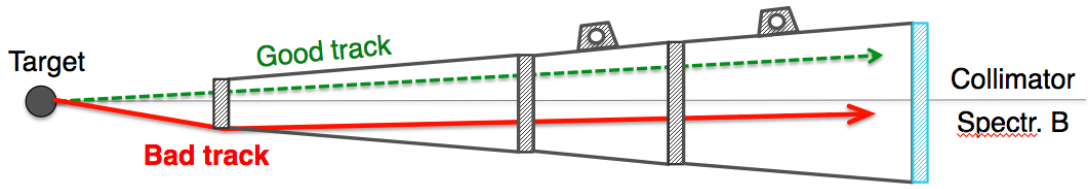

Figure 9 — Metal entrance flange of spectrometer B, which connects the scattering chamber and the magnet. Good inelastically scattered events, shown with green dashed line, are flying from target to the collimator without hitting any metal parts. Red line shows elastic which are a priori outside the momentum acceptance of the spectrometer. These events hit the think metal pieces of the snout, where they undergo the secondary scattering process and reenter spectrometer's acceptance with smaller momenta and different angles, constituting an unwanted background.

In spite of these handicaps the 2013 experiment brings important new results (see Figs. 11 and 13). A better than 1 % agreement between the data and simulation in a region of the tail, that extends even more than 200 MeV from the elastic line, demonstrates for the first time, that the the radiative corrections are understood to a sub percent level, which is essential for all future precision measurements. Furthermore, form-factors extracted from the measured tail (see Fig. 13) are in a good agreement with the values from the previous experiments, which proves, that ISR approach is a valid technique for measuring form-factors at low Q^2. Experiment also provided form-factors in the region $1 \cdot 10^{-3}\,(\mathrm{GeV}/c)^2 \leq Q^2 \leq 4 \cdot 10^{-3}\,(\mathrm{GeV}/c)^2$ where no measurements existed before. Unfortunately is the present systematic uncertainty, which is dominated by the backgrounds from the spectrometer's snout, still too large to make a significant contribution to the proton radius puzzle. However, knowing that method works has been a strong motivation for finding a way to remove the limiting background and for proposing a next generation experiment, that is presented next.

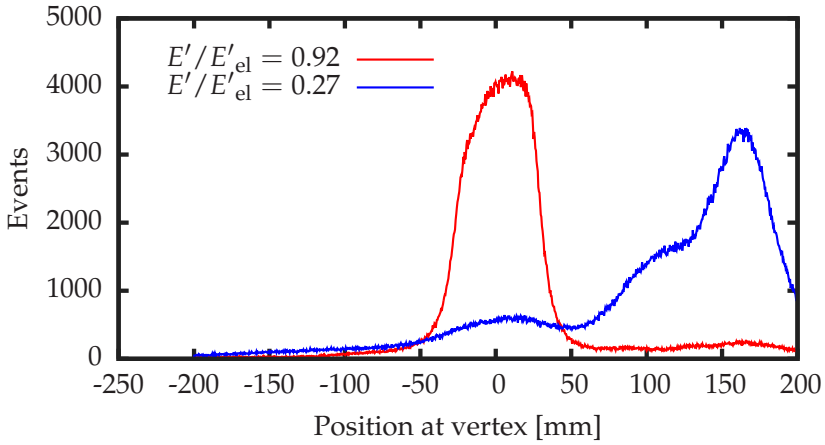

Figure 10 — Reconstructed position of events at the vertex for 195 MeV setting. When close to the elastic setting (red line) the spectrum can be clearly reconstructed with only minor contributions from the spectrometers entrance flange, visible at $z_{\mathrm{Vertex}} > 50\,\mathrm{mm}$. When measuring far away from the elastic line (blue), only small portion of events is still coming from the target. Majority of evens are artefacts from the snout and completely ruin the extraction of the form-factors.

2.4 Improvements for the next experiment

In order to be able to reduce the systematic uncertainty to 0.2 % and to reach the Q^2 of $2 \cdot 10^{-4}\,(\mathrm{GeV}/c)^2$ the backgrounds originating from the target and spectrometer's entrance flange need to be removed. This can be achieved by measuring with the gaseous jet target and by replacing the spectrometer's metal snout with a thin plastic ballon filled with Helium.

2.4.1 Hypersonic jet target

The target is being developed for the MAGIX experiment at MESA. However, its modular design allows us to use it also in the experiments at the A1. This target consists of a hyper-sonic gas jet produced by a laval nozzle (operated at a pressure of 15 bar with a minimal diameter of 1mm) and has a diameter at the target spot of 2-3mm. The gas flow is pumped by a catcher system and corresponding roots pumping systems. A conventional design of this system can achieve target densities of 10^{19} particles per square centimetre or $1 \cdot 10^{-4}\,\mathrm{g/cm^3}$. Assuming maximum MAMI current of $100\,\mu\mathrm{A}$, luminosity $1.2 \cdot 10^{34}\,/\mathrm{cm^2 s}$ can be achieved at the A1.

Without extensive metal frame in the vicinity of the vertex and no target walls, this target will offer measurements of the cross-section without unwanted backgrounds. Furthermore, a use of an effective point-like target makes the experimental results less sensitive to the shortcomings of the track reconstruction in the spectrometer.

2.4.2 Helium balloon

The limiting background of the last experiment were elastic events, which scattered one more time in the thick metal parts of the entrance flange of the spectrometer B and found their way back into spectrometers acceptance. In the analysis these events can not be separated from the good events coming from the target, because of spectrometer's inability to distinguish events along the vertical axis. Hence, to minimise this background the evacuated snout of the spectrometer

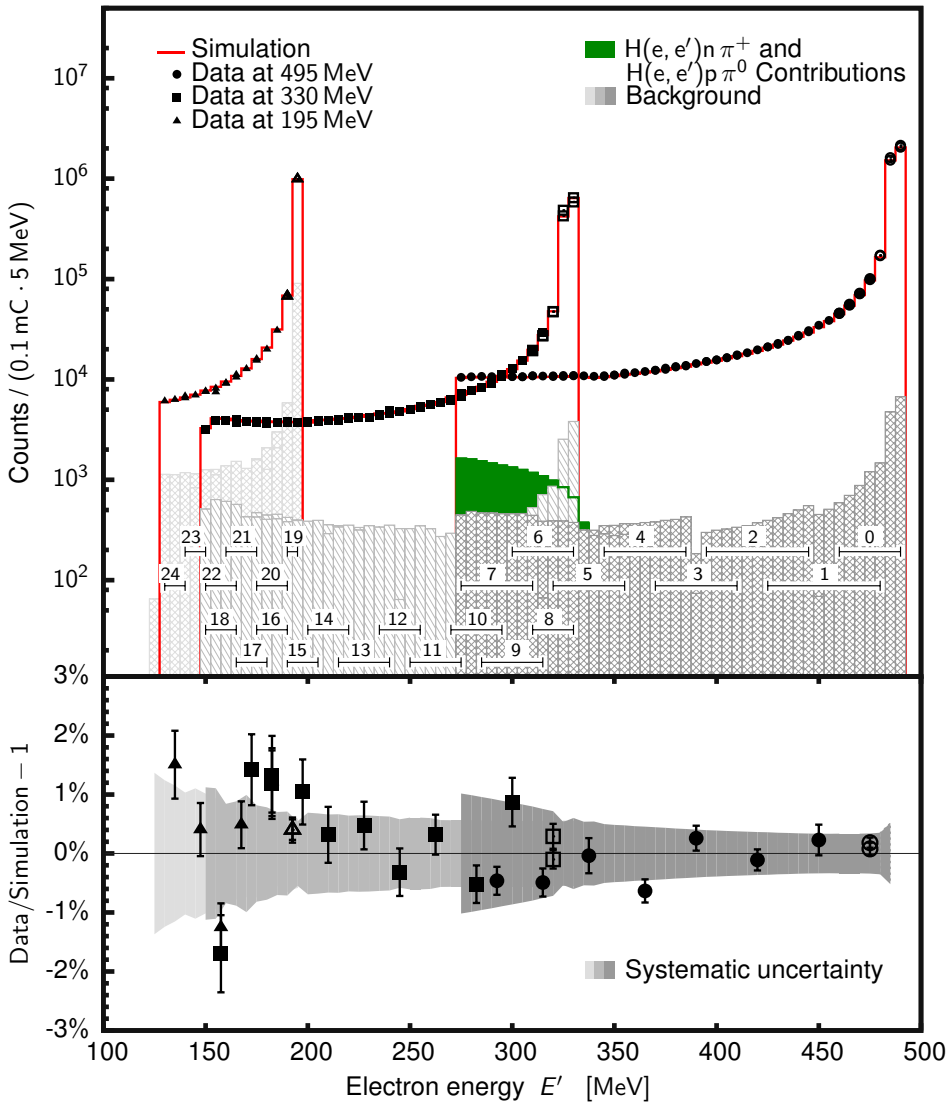

Figure 11 — Comparison of the data to the simulation. (top) Circles (squares, triangles) show the measured distributions for the 495 MeV (330 MeV, 195 MeV) setting, normalized to 0.1 mC. The elastic peak is followed by a long radiative tail. The simulation performed with form-factor parameterization of [20] is shown with a red line. The measurements at 495 MeV, 330 MeV, 195 MeV were divided into eight $(0-7)$, eleven $(8-18)$ and six $(19-24)$ energy ranges, respectively, such that two neighboring settings overlap for $1/2$ of the energy acceptance. The residual contributions of target walls and cryogenic depositions are shown with dashed fields. The full fields represent the effects of the pion production processes. (bottom) Relative difference between the data and simulation. The points show the mean values for each kinematic point, while the error bars on the points denote the statistical uncertainty of the mean value. Gray bands demonstrate the systematical uncertainties.

B will be replaced with a plastic cone, that will connect scattering chamber and spectrometer's magnet. The cone will be filled with helium at the atmospheric pressure in order for the balloon to retain the designated shape. Due to a long radiation length of a helium gas, $X_0 = 570\,\text{km}$, is the expected deterioration of the spectrometers resolution $\leq 1\,\text{mrad}$, which is less than its nominal resolving capability of 3 mrad.

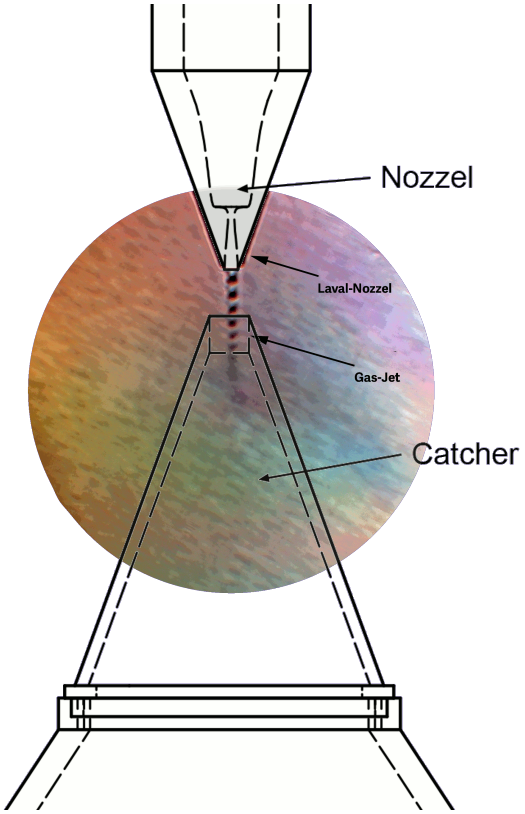

Figure 12 — Front: A schematic drawing of a windowless jet target developed for experiments at A1 and MESA. This target consists of a special nozzle that produces a hypersonic jet of hydrogen with densities of 10^{19} particles per square centimeter. The gas injected into the beam-line is then caught by the catcher system, which is located directly beneath the nozzle and is equipped with powerful vacuum-pumps. Back: A photo of hypersonic jet created with the prototype target. The photo was made with a diffraction camera.

2.5 Proposed kinematics and beam-time requests.

For the next experiment we propose measurements in the same Q^2 range but with a modified set of the kinematic points shown in Table 1 and Fig. 13. At 495 MeV the measurements will be done for six settings covering the momenta from the elastic line down to $p' = 334\,\mathrm{MeV}/c$. This is different than in the original experiment, where the 495 MeV setup consisted of eight configurations with momenta down to $p' = 290\,\mathrm{MeV}/c$. This change was made to avoid contributions of the pion production processes, which in the skipped settings contribute up to 10 % of the statistics and alone contribute 0.5 % to the systematic uncertainty. To compensate for the missing settings in the given Q^2 range, additional seven settings at 400 MeV are introduced covering the momenta down to $p' = 250\,\mathrm{MeV}/c$. These measurements are then followed by eleven and nineteen kinematic points at the 330 MeV, 195 MeV, respectively. The configurations of the last two energy settings are identical to the setups from the previous experiment. The last setting is chosen to be at the smallest momentum, $p' = 52\,\mathrm{MeV}/c$, where the magnetic field of the spectrometer B can still be measured with the 10^{-4} accuracy using NMR probe.

With the proposed kinematic configurations are the radiative tails of all four energy settings are 150 MeV long. Settings are chosen such that two neighbouring settings overlap for one half of the momentum acceptance for a precise control over the systematic uncertainty. Furthermore, the measurement is designed such, that after recording the whole radiative tail, the elastic setting is recorded one more time as gives an additional check of the stability of the apparatus.

Low target density and measurement at high currents ($\geq 5\,\mu$A) significantly improve the precision of the current measurements with fluxgate magnetometer, which was unreliable during the last low-current-measurement. However, instable density of the gaseous jet target makes determination of the luminosity to a sub-percent level still impossible. Therefore, as in the previous experiment, the spectrometer A will be used to directly monitor the relative integrated

Table 1 — Proposed kinematic settings with estimated DAQ rates ν_{DAQ} and needed time.

Setting	E_0 [GeV]	p' [GeV/c]	Q^2 [GeV$^2/c^2$]	ε	$\tau/\varepsilon\mu^2$ [%]	$G_D(Q^2)$	ν_{DAQ} [Hz]	Time [h]	Events [10^3]
ISR-495-00	0.495	0.4859	0.01706	0.965	3.91%	0.9536	458	6.5	4122
ISR-495-01	0.495	0.4470	0.01442	0.965	3.31%	0.9606	60	2.83	540
ISR-495-02	0.495	0.4157	0.01247	0.965	2.86%	0.9658	23	5.33	414
ISR-495-03	0.495	0.3866	0.01078	0.965	2.47%	0.9703	15	7.83	405
ISR-495-04	0.495	0.3596	0.00931	0.965	2.14%	0.9743	12	10.33	432
ISR-495-05	0.495	0.3344	0.00805	0.965	1.85%	0.9777	9	12.83	405
ISR-400-00	0.400	0.3924	0.01110	0.965	2.55%	0.9695	450	6.5	4050
ISR-400-01	0.400	0.3610	0.00939	0.965	2.15%	0.9741	81	2.83	729
ISR-400-02	0.400	0.3357	0.00811	0.965	1.86%	0.9775	34	3.83	428.4
ISR-400-03	0.400	0.3122	0.00701	0.965	1.61%	0.9805	23	5.33	414
ISR-400-04	0.400	0.2903	0.00606	0.965	1.39%	0.9831	17	7.33	428.4
ISR-400-05	0.400	0.2700	0.00524	0.965	1.20%	0.9854	14	8.83	428.4
ISR-400-06	0.400	0.2511	0.00453	0.965	1.04%	0.9874	12	10.33	432
ISR-330-00	0.330	0.3259	0.00765	0.965	1.75%	0.9788	450	6.5	4050
ISR-330-01	0.330	0.2998	0.00647	0.965	1.48%	0.9820	132	3.83	1663.2
ISR-330-02	0.330	0.2788	0.00559	0.965	1.28%	0.9844	51	10.33	1836
ISR-330-03	0.330	0.2593	0.00483	0.965	1.11%	0.9865	33	15.33	1782
ISR-330-04	0.330	0.2411	0.00417	0.965	0.96%	0.9883	24	20.33	1728
ISR-330-05	0.330	0.2242	0.00361	0.965	0.83%	0.9899	20	22.83	1620
ISR-330-06	0.330	0.2085	0.00312	0.965	0.72%	0.9913	17	22.83	1377
ISR-330-07	0.330	0.1939	0.00270	0.965	0.62%	0.9924	15	25.33	1350
ISR-330-08	0.330	0.1803	0.00233	0.965	0.53%	0.9935	14	25.33	1260
ISR-330-09	0.330	0.1676	0.00201	0.965	0.46%	0.9944	13	25.33	1170
ISR-330-10	0.330	0.1559	0.00174	0.965	0.40%	0.9951	12	25.33	1080
ISR-195-00	0.195	0.1936	0.00269	0.965	0.62%	0.9925	450	6.5	4050
ISR-195-01	0.195	0.1781	0.00227	0.965	0.52%	0.9936	360	2.83	3240
ISR-195-02	0.195	0.1656	0.00196	0.965	0.45%	0.9945	133	2.83	1197
ISR-195-03	0.195	0.1540	0.00170	0.965	0.39%	0.9952	87	3.83	1096.2
ISR-195-04	0.195	0.1432	0.00147	0.965	0.34%	0.9959	65	5.33	1170
ISR-195-05	0.195	0.1331	0.00127	0.965	0.29%	0.9964	52	6.33	1123.2
ISR-195-06	0.195	0.1238	0.00110	0.965	0.25%	0.9969	45	7.33	1134
ISR-195-07	0.195	0.1151	0.00095	0.965	0.22%	0.9973	40	8.33	1152
ISR-195-08	0.195	0.1070	0.00082	0.965	0.19%	0.9977	37	9.33	1198.8
ISR-195-09	0.195	0.0995	0.00071	0.965	0.16%	0.9980	34	9.33	1101.6
ISR-195-10	0.195	0.0925	0.00061	0.965	0.14%	0.9983	32	10.33	1152
ISR-195-11	0.195	0.0860	0.00053	0.965	0.12%	0.9985	31	10.33	1116
ISR-195-12	0.195	0.0800	0.00046	0.965	0.10%	0.9987	30	10.33	1080
ISR-195-13	0.195	0.0744	0.00040	0.965	0.09%	0.9989	30	10.33	1080
ISR-195-14	0.195	0.0692	0.00034	0.965	0.08%	0.9990	30	10.33	1080
ISR-195-15	0.195	0.0643	0.00030	0.965	0.07%	0.9992	30	10.33	1080
ISR-195-16	0.195	0.0598	0.00026	0.965	0.06%	0.9993	30	10.33	1080
ISR-195-17	0.195	0.0556	0.00022	0.965	0.05%	0.9994	30	10.33	1080
ISR-195-18	0.195	0.0517	0.00019	0.965	0.04%	0.9995	30	10.33	1080

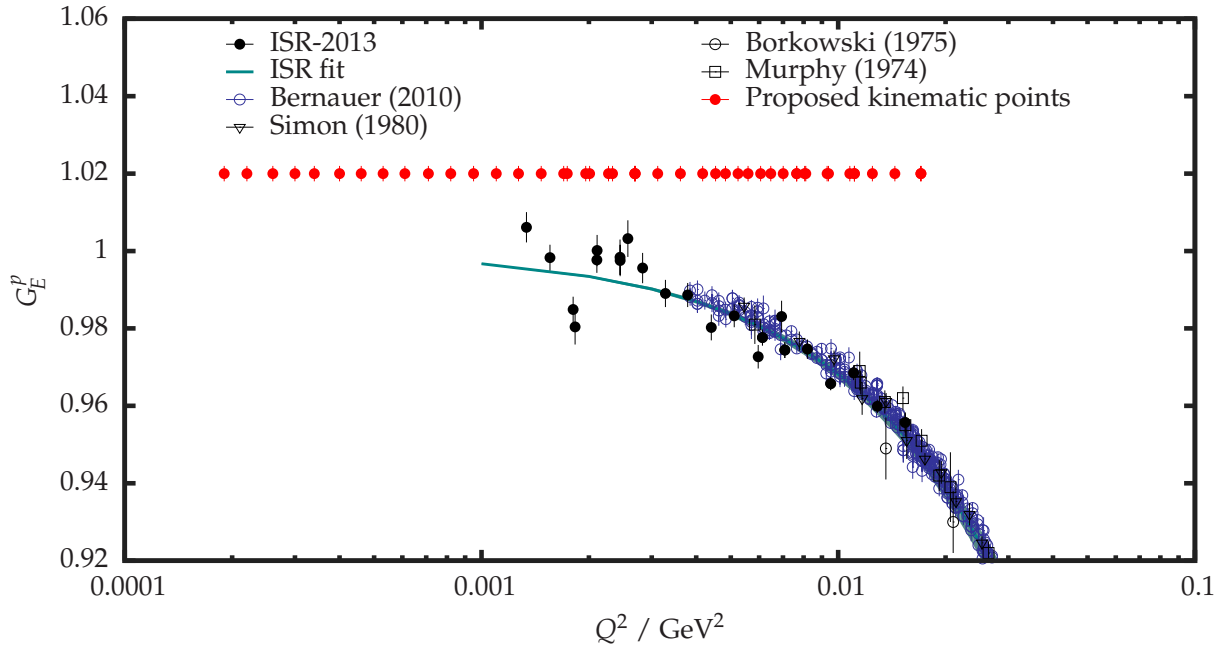

Figure 13 — Proposed kinematic points with the anticipated statistical uncertainties. Plot also shows older measurements in this Q^2 range (see Fig. 2) and preliminary results of the 2013 ISR experiment, that are just being finalised. Cyan line shows the fit to the ISR data.

Table 2 — Expected rates in spectrometer A.

Setting	E_0 [GeV]	E' [GeV]	θ_e [°]	Raw rate in B [Hz]	Raw rate in A [Hz]
ISR-495-00	0.495	0.462	30	457	100
ISR-400-00	0.400	0.378	30	725	167
ISR-330-00	0.330	0.315	30	1085	260
ISR-195-00	0.195	0.190	30	3218	836

luminosity with a 0.2 % precision. The expected rates in spectrometer A with respect to the rates in spectrometer B as a function of a scattering angle are shown Fig. 15 . In order to collect enough statistics for a proper normalisation of the ISR spectra, spectrometer A should be positioned at small angles. However, at most forward angles, the quadrupole magnet of spectrometer A starts distorting spectra in spectrometer B. In order to minimise these effects while trying to keep rates high, an angle of 25° was selected as a optimal position for spectrometer A. Expected rates are gathered in Table 2.

To provide valuable contribution to the proton radius problem the experiment aims to measure the proton charge form-factor with the 0.2 % statistical uncertainty. Assuming beam current of 20 μA and luminosity of $2.4 \cdot 10^{33}$ /cm^{2}s, acquisition rates between 10 Hz and 30 Hz are expected in the spectrometer B, when measuring in the tail region. On the other hand, the maximum rate at the elastic peak is limited to 450 Hz by the capability of the Data Acquisition System (DAQ). The predicted rates for every setting are shown in Table 1 and Fig. 14. With these rates 22 full days are required to accomplish the program including the time needed to change the configurations. Considering also the time needed for maintenance of the accelerator and few extra days for resolving malfunctions of equipments, such as water leaks and failures in the electronics, we therefore ask for 30 days of beam-time.

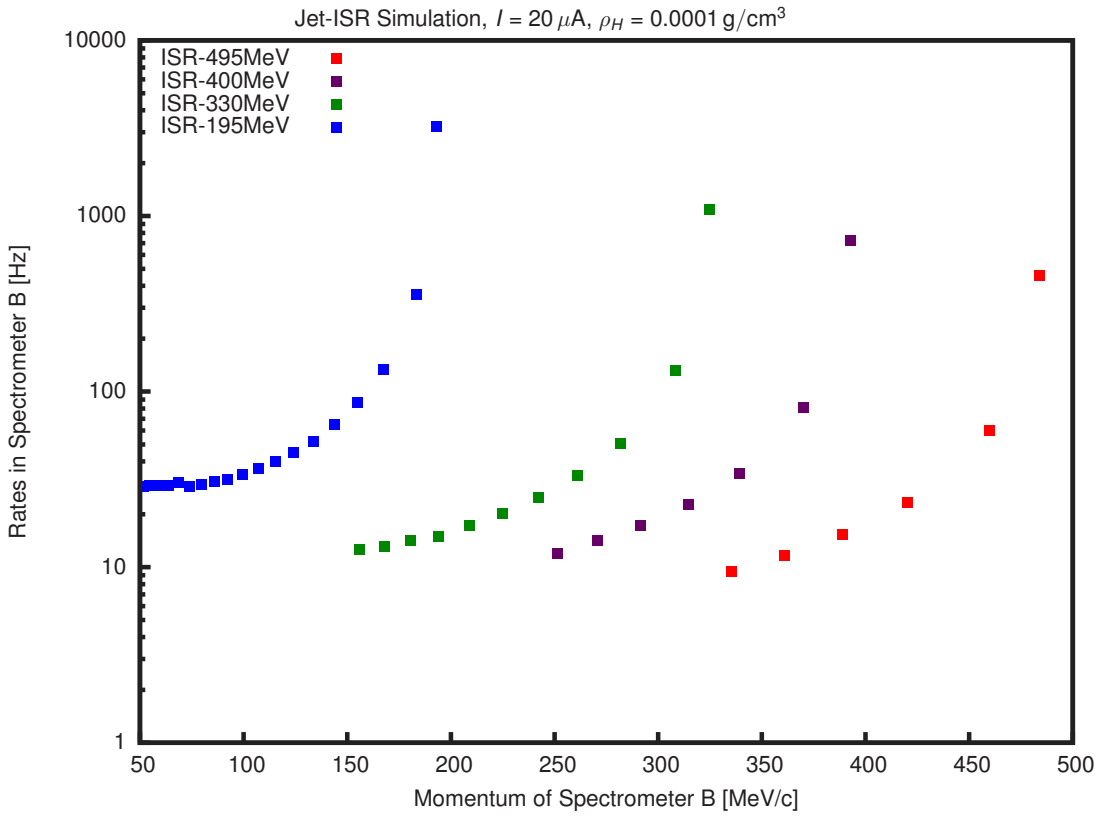

Figure 14 — Predicted raw rates for the kinematic settings summarised in Table 1 assuming target density of $0.0001\,\mathrm{g/cm^3}$ and beam current of $20\,\mu$A. Experiment proposes measurements at four different beam energies: 195 MeV, 330 MeV, 400 MeV and 495 MeV. The expected rates are always below the capability of the DAQ, except for the elastic settings. There the raw rates will be prescaled to keep the acquisition rate below the maximum of 450 Hz.

2.6 Systematic uncertainty

An advantage of the ISR technique is extremely good control over the systematic uncertainties. With the fixed angular setting and overlapping momentum ranges all ambiguities related to the acceptances disappear. Furthermore, with spectrometer A one directly measures the luminosity, thus avoiding potential problems with fluctuations in beam current and target density, leading to a relative luminosity determination with an accuracy better than 0.17 %. The only other sources of systematic uncertainty are the ambiguity in the determination of detector efficiencies of 0.2 % and the contributions of the higher order corrections to the simulation (see Fig. 16), which are not included in the simulation and are estimated to 0.6 %. Summed in squares is the total systematic uncertainty estimated to 0.65 % and is of the same size as the systematic uncertainty of the best present results at 495 MeV. However, with improvements in the theoretical calculations, that are already being developed, will this uncertainty be further reduced.

References

[1] R. W. McAllister and R. Hofstadter, Phys. Rev. **102** , 851 (1956).

[2] R. Pohl *et al.*, Nature **466**, 213 (2010).

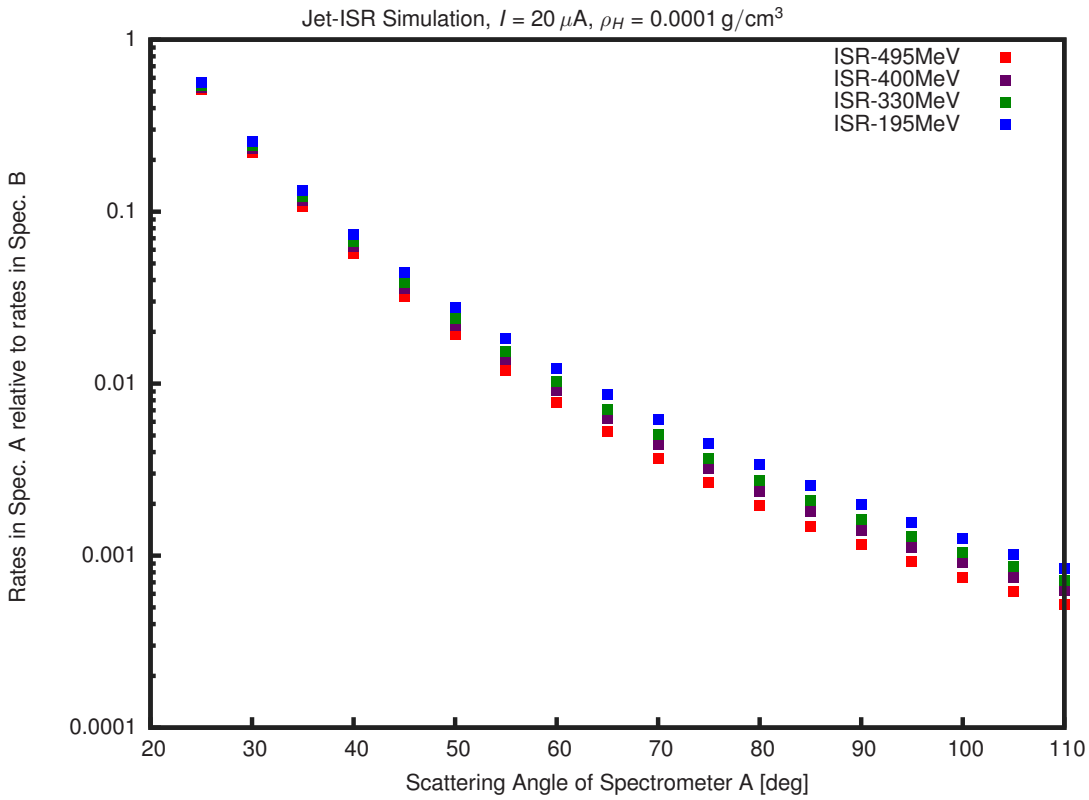

Figure 15 — The predicted rates for the spectrometer A as a function of the scattering angle for the four considered beam energies: 195 MeV, 330 MeV, 400 MeV and 495 MeV. Rates are shown relative to the raw rates in the spectrometer B assuming elastic peak always in the middle of the acceptance of spectrometer A.

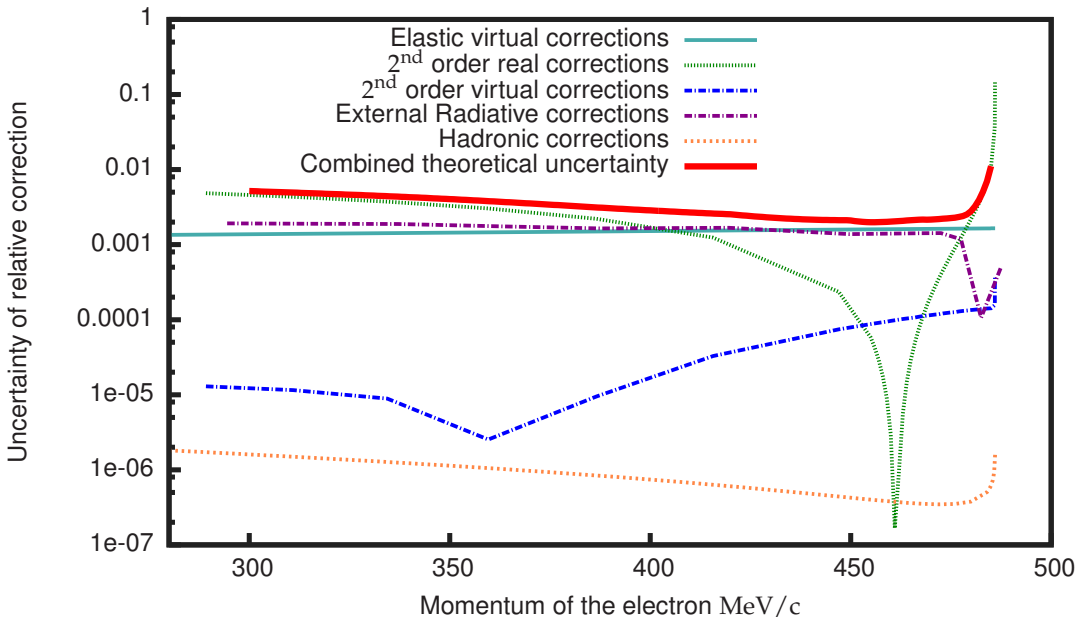

Figure 16 — Absolute uncertainties of the next-to-leading order corrections presented in the Fig. 6. The thick red line shows the full theoretical uncertainty as a function of particle's momentum for the 495 MeV setting.

[3] A. Antognini *et al.*, Science **339**, 417 (2013).

[4] J. Beringer *et al.* (Particle Data Group), Phys. Rev. D **86**, 010001 (2012).

[5] R. Pohl *et al.*, Science **353**, 6300, 669 (2016).

[6] A. Antognini *et al.*, Annals of Physics **331**, 127 (2013).

[7] F. Hagelstein *et al.*, Prog. Part. Nucl. Phys. **88** 29 (2016).

[8] J. C. Martens, J. P. Ralston, arXiv:1606.06209 [hep-ph] (2016).

[9] H. Merkel *et al.*, Phys. Rev. Lett. **112**, 221802 (2014).

[10] M. N. Rosenbluth, Phys. Rev. **79**, 615 (1950).

[11] M. Mihovilovič *et al.*, EPJ Web of Conferences **72**, 00017 (2014).

[12] L. N. Hand *et al.*, Rev. Mod. Phys. **35**, 335 (1963).

[13] D. Frerejacque *et al.*, Phys. Rev. **141**, 1308 (1966).

[14] Yu. K. Akimov *et al.*, JETP **35**, 651 (1972).

[15] F. Borkowski *et al.*, Nucl. Phys. A **222**, 269 (1974).

[16] G. G. Simon *et al.*, Nucl. Phys. A **333**, 381 (1980).

[17] M. McCord *et al.*, Nucl. Instrum. Meth. B **56/57**, 496 (1991).

[18] I. Eschrich *et al.*, Phys. Lett. B **522**, 233 (2001).

[19] J. J. Murphy *et al.*, Phys. Rev. C **9**, 2125 (1974).

[20] J. C. Bernauer *et al.*, Phys. Rev. Lett. **105**, 242001 (2010).

[21] J. C. Bernauer *et al.*, Phys. Rev. C **90**, 015206 (2014).

[22] Th. Pospischil *et al.*, Eur. Phys. J. A **12**, 125 (2001).

[23] G. Ron *et al.*, Phys. Rev. Lett. **99**, 202002 (2007).

[24] X. Zhan *et al.*, Phys. Lett. B **705**, 59 (2011).

[25] J. Arrington, I. Sick, arXiv:1505.02680v1 [nucl-ex] (2015).

[26] G. Ron *et al.*, Phys. Rev. C **84**, 055204 (2011).

[27] I. Sick *et al.*, Prog. Part. Nucl. Phys. **67**, 473 (2012).

[28] C. Adamuscin *et al.*, Prog. Part. Nucl. Phys. **67**, 479 (2012).

[29] I. T. Lorentz *et al.*, Phys. Rev. D **91**, 014023 (2015).

[30] K. Griffioen *et al.*, Phys. Rev. C **93**, 065207 (2016).

[31] D. W. Higinbotham *et al.*, Phys. Rev. C **93**, 055207 (2016).

[32] M. O. Distler *et al.*, arXiv:1511.00479 [nucl-ex] (2015).

[33] J. C. Bernauer *et al.*, arXiv:1606.02159 [nucl-th] (2016).

[34] I. Sick, D. Trautmann, Phys. Rev. C **89** ,012201(R) (2014).

[35] W. Lamb Jr. *et al.*, Phys. Rev. **72**, 241 (1947).

[36] R. Pohl *et al.*, Annu. Rev. Nucl. Part. Sci. **63**, 175 (2013).

[37] M. Meziane *et al.*, AIP Conf. Proc. **1563**, 183 (2013).

[38] R. Gilman *et al.*, arXiv:1303.2160 [nucl-ex] (2013).

[39] B. Aubert *et al.*, Phys. Rev. D **69**, 011103(R) (2004).

[40] M. Vanderhaeghen *et al.*, Phys. Rev. C **62**, 025501 (2000).

[41] J. M. Friedrich, PhD Thesis (2000).

[42] T. Beranek, Private communication.

[43] Y.-S. Tsai, Phys. Rev. **122**, 1898 (1960).

[44] L. W. Tsai, Y. S. Tsai, Rev. Mod. Phys. **41**, 205 (1969).

[45] L. C. Maximon J. A. Tjon, Phys. Rev. C **62**, 054320 (2000).

[46] K. I. Blomqvist *et al.*, Nucl. Instr. Meth. Phys. Res. A **403**, 263 (1998).